Experimental Study on Hydrodynamic Characteristics of a Disk-Shaped Buoy Using a Large-Scale Wave Flume

Zhonghua Tan , Hanbao Chen * , Songgui Chen , Ning Guan * , Yingni Luan , Wenjun Shen

Posted Date: 14 May 2026

doi: 10.20944/preprints202605.0930.v1

Keywords: disk-shaped buoy; large-scale wave flume; physical model experiment; hydrodynamic analysis; scale effects

 doi:10.20944/preprints202605.0930.v1

Article

Experimental Study on Hydrodynamic Characteristics of a Disk-Shaped Buoy Using a Large-Scale Wave Flume

Zhonghua Tan [1,2], Hanbao Chen [2,*], Songgui Chen [2], Ning Guan [2,*], Yingni Luan [2] and Wenjun Shen [2,]

[1] Ocean University of China, Qingdao 266003, China

[2] Tianjin Research Institute for Water Transport Engineering, National Engineering Laboratory for Port Hydraulic Construction Technology, Tianjin 300456, China

* Correspondence: chensg05@163.com (S.C.); guanning_tj@163.com (N.G.);

Abstract

A systematic experimental investigation was conducted on the motion response (RAO) and mooring performance of a novel disk-shaped buoy (geometric scale 1:10) subjected to combined wind, wave, and current actions. A hybrid experimental strategy was employed, integrating a large-scale wave flume (for long-period waves and currents) with a harbor basin (for short-period waves and wind), aiming to mitigate the scale effects inherent in Froude-scaled models, particularly with regard to drag force measurements. The test matrix included free decay in calm water, RAOs under regular waves, motion and mooring line tension under irregular waves, and measurements of wind and current drag coefficients. Key results indicate a natural roll period of approximately 3.0 s with a notably high dimensionless damping ratio ($\zeta \approx 0.14$–0.15), which is conducive to rapid motion attenuation. A pronounced resonance peak in the roll RAO (26.6°/m) was observed near the 3 s period. Under an extreme sea state ($H_s = 13.8$ m, $T_p = 16.1$ s), the maximum roll angle and dynamic mooring line tension reached 21.30° and 61.56 kN, respectively, the latter being about 3.0 times the static pretension. The mean wind drag coefficient and current drag coefficient were determined as 0.76 and 0.44. This research provides a validated dataset and critical insights for the design, mooring system optimization, and operational safety assessment of such disk-shaped buoys. The effectiveness of the hybrid testing approach is confirmed, and the favorable damping characteristic of this buoy form is highlighted.

Keywords: disk-shaped buoy; large-scale wave flume; physical model experiment; hydrodynamic analysis; scale effects

1. Introduction

With the continuous advancement of global marine development activities, ocean buoys have become increasingly important as critical infrastructure for marine environmental monitoring, disaster warning, maritime traffic safety, and marine resource exploitation [1]. Ocean buoys are capable of long-term, continuous, fixed-point, all-weather operations in harsh marine environments, providing essential data support for marine scientific research, resource development, and environmental protection. According to their application scenarios and functional requirements, ocean buoys can be classified into various types, including meteorological observation buoys, water quality monitoring buoys, wave measurement buoys, navigation buoys, and auxiliary buoys for marine energy development [2]. However, when operating under complex ocean conditions (combined wind, wave, and current actions), the motion responses and load characteristics of buoys exhibit strong complexity and nonlinearity, which imposes increasingly stringent requirements on buoy structural design, mooring system optimization, and operational safety. In recent years, wave

 doi:10.20944/preprints202605.0930.v1

energy marine buoys, as an emerging platform for ocean observation and energy utilization, have received widespread attention [3].

The hydrodynamic characteristics of buoys directly govern their operational stability and measurement accuracy. The roll, pitch, and heave motion responses determine the working precision and reliability of onboard equipment (such as radar, communication antennas, and optical sensors), whereas the dynamic tension of the mooring system relates to the survivability of the buoy in extreme sea states and the safety of long-term operation [4]. Roll damping is a critical parameter affecting the motion stability of floating bodies and the dynamic loads on mooring systems; radiation damping theory provides an essential foundation for analyzing floating body motion responses [5]. High damping characteristics are conducive to suppressing resonant responses [6,7]. Consequently, in-depth investigation of buoy hydrodynamic characteristics, together with accurate acquisition of motion response patterns, damping characteristics, and environmental load coefficients, is of considerable theoretical significance and engineering value for buoy optimization design, mooring system selection, and safe operation assessment.

Currently, research on buoy hydrodynamic characteristics has made considerable progress, with research methods mainly including theoretical analysis, numerical simulation, physical model experiments, and field observations [1]. In terms of theoretical analysis, Duggal and Ryu et al. [8,9] employed coupled nonlinear time-domain methods to predict the motion response of deepwater buoys; Le Cunff et al. [10] derived frequency-domain calculation methods, providing a theoretical basis for rapid assessment of buoy dynamic response; Salem et al. [11] used various linearization methods to solve the equations of motion, effectively addressing the nonlinear damping issues of mooring systems. Numerical methods have demonstrated favorable accuracy and efficiency in predicting the motion response of buoys in regular waves [12].

In terms of numerical simulation, commercial software such as AQWA, Fluent, RecurDyn, Orcaflex, and SESAM have been widely applied. Lu et al. [13] and Zhu et al. [14] used AQWA software for frequency-domain and time-domain analysis to study the influence of different mooring systems on buoy hydrodynamic performance; Chang et al. [15] utilized RecurDyn software to model the buoy deployment process, providing theoretical support for buoy design and optimization; Zheng et al. [3] established a deep-sea single-point meteorological buoy model using Orcaflex software to investigate the dynamic response characteristics of the system to sea state parameters and structural parameters. In addition, Li et al. [16] conducted detailed analyses of the six-degree-of-freedom motion response of large marine data buoys under different sea states using a DES-VOF coupled method, finding deviations of less than 10% compared with experimental results, which validates the reliability of numerical simulation in buoy hydrodynamic analysis.

In terms of physical model experiments, researchers simulate marine environments in wave basins or flumes using scaled buoy models. Hegde et al. [17] investigated spar-buoy platforms with heave plates through wave basin experiments and numerical simulations, finding that configurations with plates near the free surface reduced peak heave response by approximately 75% and pitch response by around 30%. Zhu et al. [18] experimentally examined the motion suppression effects of heave plates on cylindrical floating structures, demonstrating that heave plates significantly increase added mass and reduce peak heave RAO by about 40%. Capobianco et al. [19] conducted wave basin tests on cylindrical buoys to assess the influence of different disc configurations on wave measurement accuracy. Although heave plates are extensively employed for motion suppression of floating bodies [17,18], disc-shaped buoys themselves can generate pronounced radiation damping effects through their distinctive geometric characteristics, which differs from the added damping mechanism of heave plates. Investigations into the hydrodynamic characteristics of flat plate structures provide valuable reference for understanding the radiation damping mechanism of disc-shaped buoys [20]. Domestically, the research team at the National Ocean Technology Center validated the stability of anchor system designs [21]; Cao et al. [22] verified the validity of numerical simulation results; and Zhang et al. [23] corrected the damping matrix in simulation models through model experiments. Regarding field observations of buoy hydrodynamic characteristics, Eriksson et

 doi:10.20944/preprints202605.0930.v1

al. [24,25] from Uppsala University, Sweden, conducted full-scale experiments on column-type moored buoys at a wave energy research test site, confirming the accuracy of computational models based on potential flow theory. Yuan et al. [26] systematically investigated the hydrodynamic performance of an OWC wave energy converter in a wave flume, demonstrating that the spring-like effect of air compressibility significantly influences the energy capture efficiency, with their experimental methodology providing valuable reference for large-scale buoy hydrodynamic tests.

Despite the fruitful achievements of existing research, some shortcomings remain. First, traditional small-scale model experiments (typically with scales of 1:50-1:100) are limited by Froude similarity criteria and cannot simultaneously satisfy Reynolds number similarity, resulting in significant scale effects on viscosity-related drag coefficients and damping characteristics, which affects the accuracy of experimental results [27,28]. Second, numerical simulation methods still face challenges when dealing with strongly nonlinear problems (such as large-amplitude motion, vortex shedding, flow separation, etc.), and model validation requires high-quality experimental data support [29]. Furthermore, field measurements are costly, time-consuming, and subject to uncontrollable sea states, making it difficult to systematically obtain complete hydrodynamic characteristics of buoys under various sea conditions [30].

Large-scale wave flume experiments serve as an important bridge connecting small-scale model experiments with field measurements, offering unique advantages in reducing scale effects and improving experimental accuracy. In recent years, significant progress has been made in the construction of large-scale wave flumes worldwide, such as the large-scale wave flume at Tianjin Research Institute for Water Transport Engineering (TIWTE) in China (456 m long, 5 m wide, 12 m deep), the Delta Flume at Deltares in the Netherlands (300 m long, 5 m wide, 9.5 m deep), and the Large Wave Flume at Leibniz University Hannover in Germany (310 m long, 5 m wide, 7 m deep) [27,31]. These large-scale testing facilities enable experiments with model scales of 1:10 or even larger, significantly increasing the model Reynolds number and bringing the flow into or near the self-similarity region, thereby effectively reducing the impact of scale effects on drag coefficients and damping characteristics [32,33]. To the best of the authors' knowledge, no systematic study has been reported on the hydrodynamic characterization of disk-shaped buoys using large-scale wave flume facilities, particularly under combined wind-wave-current conditions. This represents a significant knowledge gap, as the scale effects inherent in small-scale tests (1:50–1:100) may lead to substantial underestimation of damping coefficients and drag forces, thereby compromising the reliability of design parameters for full-scale applications. Specifically, the large beam-to-draft ratio ($D/T \approx 10$) and shallow-draft geometry of disk-shaped buoys render their roll damping characteristics particularly sensitive to Reynolds number scaling, whereas the blunt-body flow separation pattern around the disc hull introduces scale-dependent nonlinearities in drag force measurements that are difficult to capture in conventional small-scale wave basins. Furthermore, the coupled wind-wave-current excitation conditions, which represent the most critical operational and survival scenarios for such buoys, have not been systematically examined in large-scale experimental settings. Consequently, there is an urgent need for systematic experimental investigations utilizing large-scale wave flume facilities to provide reliable hydrodynamic datasets for this class of buoy systems.

In view of this, this study employs a hybrid experimental method combining a large-scale wave flume (for long-period waves and current) with a harbor basin (for short-period waves and wind) to systematically investigate the motion response and mooring performance of a novel disk-shaped buoy (geometric scale 1:10) under combined wind, wave, and current actions. This method aims to reduce the inherent scale effects of Froude-scaled models, particularly concerning drag force measurements, to obtain more accurate buoy hydrodynamic characteristic parameters. The research contents include: (1) free decay tests in calm water to identify the natural period and damping characteristics of the buoy; (2) regular wave RAO tests to obtain the buoy motion response amplitude operators; (3) irregular wave tests to evaluate the motion and cable tension response under moderate and extreme sea states; and (4) wind/current drag coefficient measurements to provide key parameters for mooring system design.

 doi:10.20944/preprints202605.0930.v1

The contributions of this study are threefold: First, it validates the effectiveness of the hybrid testing approach combining large-scale wave flume and harbor basin for buoy hydrodynamic characterization. Second, it reveals the high roll damping characteristic ($\zeta \approx 0.14$-0.15) of the disk-shaped buoy, which is favorable for motion stability. Third, it provides a comprehensive dataset including RAOs, extreme sea state responses, and environmental load coefficients, offering critical insights for the design and operation of similar buoys.

2. Methods

2.1. Model Design

2.1.1. Similarity Criteria

The objective of the present experiment is to simulate the dynamic responses of a buoy subjected to combined wind, wave, and current actions. Therefore, the gravity similarity criterion, i.e., Froude similarity, was adopted as the primary scaling law. In addition, elastic similarity was taken into account to ensure the accurate representation of the mooring system behavior. The scaling relationships of the relevant physical quantities are summarized as follows:

Geometric scale:

$$\lambda = \frac{L_r}{L_m} = 10 \tag{1}$$

Wave height scale:

$$\lambda_H = \lambda = 10 \tag{2}$$

Period (time) scale:

$$\lambda_T = \lambda^{1/2} = \sqrt{10} \approx 3.162 \tag{3}$$

Velocity scale:

$$\lambda_V = \lambda^{1/2} = \sqrt{10} \approx 3.162 \tag{4}$$

Force scale:

$$\lambda_F = \lambda^3 = 1000 \tag{5}$$

Specifically, the model design satisfies the following similarity requirements:

Geometric similarity: Strict linear scaling was maintained between the model buoy, mooring lines, and the prototype.

Static similarity: A ballast adjustment method was employed, in which ballast blocks were placed at appropriate locations inside the model to ensure that the total weight and center of gravity under the corresponding loading conditions satisfy similarity relationships with the prototype.

Dynamic similarity: The principal dynamic parameters of the buoy model, including mass moments of inertia as well as roll and pitch natural periods, were designed to conform to similarity requirements.

Elastic similarity: The force–deformation relationship of the model mooring lines was scaled to be similar to that of the prototype mooring chains, thereby ensuring an accurate representation of mooring dynamic responses.

2.1.2. Test Model

(1) Buoy Model

The buoy model was fabricated using steel and engineering plastics and manufactured in strict accordance with the geometric similarity criterion. During the fabrication process, ballast adjustment

 doi:10.20944/preprints202605.0930.v1

was applied to ensure that key physical parameters, including total mass, center of gravity, and mass moments of inertia, satisfied the similarity requirements.

Table 1 summarizes the main parameters of the buoy model. The discrepancies between the fabricated model and the corresponding theoretical values were well controlled, with the mass error less than 2%, the error in the vertical position of the center of gravity less than 2%, and the error in the mass moments of inertia less than 3%.

Table 1. Main parameters of the buoy.

Parameter	Prototype	Theoretical Model	Actual Model	Error (%)
Disc diameter (m)	10	1	1	0
Depth (m)	6	0.6	0.6	0
Draft (m)	1.035	0.104	0.106	1.9
Displacement (kg)	55700	55.7	55.7	0
Vertical center of gravity (m)	1.137	0.114	0.115	0.9
Roll moment of inertia (kg·m²)	3.777×10^5	3.777	3.767	0.3
Pitch moment of inertia (kg·m²)	3.777×10^5	3.777	3.767	0.3
Yaw moment of inertia (kg·m²)	5.091×10^5	5.091	4.992	1.9

A single-point mooring configuration was adopted in the experiment. The model mooring chain was fabricated from stainless steel. In addition to satisfying geometric similarity, particular emphasis was placed on matching the mass per unit length and stiffness characteristics of the prototype chain.

By adjusting the configuration of the model mooring chain, the mass per unit length was scaled to satisfy the gravity similarity requirement, while the elastic deformation behavior was ensured to be similar to that of the prototype. The main parameters of the mooring chain model are listed in Table 2.

Table 2. Main parameters of the mooring chain model.

Parameter	Prototype	Theoretical Model	Actual Model	Error (%)
Chain diameter (mm)	52	5.2	6	15.4
Weight per unit length (kg/m)	61.8	0.618	0.65	5.2
Total chain length (m)	150	15	15	0
Water depth (m)	50	5	5	0
Chain diameter (mm)	52	5.2	6	15.4

2.1.3. Simulation of Wave Conditions

The experiments were conducted in a large-scale wave flume and a harbor and coastal engineering basin, where a variety of wave conditions were simulated. For regular wave tests, the wave period ranged from 2.5 s to 15 s, while the wave height was scaled according to the geometric similarity ratio.

To more realistically represent marine environments, irregular wave conditions were also simulated. An improved JONSWAP spectrum proposed by Goda was adopted, with peak periods ranging from 8.5 s to 16.1 s, covering both moderate and extreme sea-state conditions.

All wave parameters were determined based on similarity criteria. Prior to the regular wave tests, the wave generation signals were iteratively adjusted to ensure that the deviations of the generated mean wave height and period from the target values were within ±5%. The free surface elevation was sampled at an interval of 0.02 s, and for each regular wave condition, more than ten complete consecutive wave cycles were recorded to ensure data stability.

For irregular wave tests, the JONSWAP spectrum was employed with a peak enhancement factor of $\gamma = 3.3$. The wave train length exceeded 100 waves to ensure sufficient statistical convergence.

 doi:10.20944/preprints202605.0930.v1

2.1.4. Simulation of Wind Conditions

Wind condition tests were conducted to simulate a range of wind speeds from 6 to 20 knots, corresponding to prototype wind speeds of approximately 10.44 m/s to 33.20 m/s. The wind speeds were scaled according to the dynamic similarity criterion to ensure the accuracy and comparability of the experimental results.

The wind load experiments were performed in the harbor and coastal engineering basin. Based on the Froude similarity law, the prototype wind speeds were scaled using a velocity scale of $\lambda_V = \lambda^{1/2} = \sqrt{10} \approx 3.162$.

Five representative prototype wind speed conditions, namely 10.44 m/s, 13.41 m/s, 21.25 m/s, 25.77 m/s, and 33.20 m/s, were simulated, covering typical operational and survival wind conditions for the buoy (as summarized in Table 8).

Wind speeds were synchronously measured and calibrated using multiple hot-wire anemometers installed upstream of the buoy model in the windward direction, ensuring uniformity and stability of the wind field within the test section. The measurement error was controlled within ±2%. The wind field was generated using a multi-fan combined system, in which the fan rotational speeds were precisely regulated by variable-frequency drives to produce the required wind speeds.

2.1.5. Simulation of Current Conditions

Current tests were conducted to simulate a range of flow velocities from 2 to 6 knots, corresponding to prototype current speeds of approximately 0.33 m/s to 0.98 m/s. The current velocities were scaled according to the dynamic similarity criterion to realistically represent the hydrodynamic loading characteristics of the buoy under different current conditions.

The simulation of current-induced loads was performed in the large-scale wave flume. Based on the Froude similarity law, the prototype current velocities were scaled using a velocity scale of $\lambda_V = \lambda^{1/2} = \sqrt{10} \approx 3.162$.

Three representative prototype current conditions, namely 2 knots, 4 knots, and 6 knots (corresponding to 1.03 m/s, 2.06 m/s, and 3.09 m/s, respectively), were simulated.

The current velocity was accurately measured using a Vectrino+ acoustic Doppler velocimeter, with a sampling frequency of 50 Hz to capture fine-scale flow variations. The measurement accuracy was ±1% of the measured value ±0.5 cm/s. A uniform current field was generated by the flume circulation system and calibrated repeatedly at the buoy model location to ensure accurate flow magnitude and direction. This provided a reliable experimental environment for the determination of the buoy current drag coefficient.

2.2. Testing Equipment and Methods

2.2.1. Test Basins

This study utilized two internationally advanced test basins in a comprehensive manner. The primary rationale for this hybrid approach was to ensure that the RAO tests remained within the linear range, where the ratio of wave height to wavelength for regular waves generated by the wavemaker is approximately 1/35 to 1/50. Considering the wave-making capabilities of the actual basins and the flume, regular wave tests for prototype periods of 2.5 s to 5.2 s were conducted in the harbor and coastal engineering basin, while those for prototype periods of 5.9 s to 15 s were performed in the large-scale wave flume.

(1)Large-scale Wave Flume

Long-period wave (prototype period 5.9~15 s) and current load tests were carried out in the large-scale wave flume at the Tianjin Research Institute for Water Transport Engineering, Ministry of Transport. This flume is 5 m wide, 456 m long, with a test section depth of 12 m. It is equipped with an advanced electro-servo driven wavemaker system capable of accurately simulating both regular and irregular waves. Its maximum achievable regular wave height is 3.5 m, with an effective wave

 doi:10.20944/preprints202605.0930.v1

period range of 2-8 seconds (model scale). Currently one of the largest and most powerful wave generation facilities in the world, it provides an ideal simulation environment for testing the motion response of the buoy under long-period waves (prototype period 5.9~15 s). An energy dissipation device is installed at the tail of the flume, effectively suppressing wave reflection and ensuring wave field quality.

(2) Harbor and Coastal Engineering Basin

Short-period wave (prototype period 2.5 ~ 5.2 s) and wind load tests were carried out in a harbor and coastal engineering basin measuring 54.0 m in length, 13.2 m in width, and 1.0 m in depth. The basin is equipped with three 4-m-wide absorbing-type irregular wavemakers, with a maximum operating water depth of 0.7 m, a wave-height range of 0–35 cm, and a wave-period range of 0.5–5.0 s (model scale), enabling accurate simulation of irregular wave trains such as those defined by the JONSWAP spectrum. In addition, the basin is fitted with a multi-fan wind-generation system. Through frequency-converter control, the system can achieve stepless speed regulation within a model-wind-speed range of 0–10.0 m/s, and the fans can be moved flexibly to simulate different wind directions.

2.2.2. Measurement Instruments

A variety of high-precision sensors and a synchronous data acquisition system were employed in the tests to perform synchronized, real-time measurements of wave surface elevation, buoy motion, forces, and environmental parameters. The main instruments used are listed in Table 3.

Table 3. Main instruments of the experimental measurement system.

Measured Quantity	Instrument Name	Measured Quantity	Instrument Name	Measured Quantity	Instrument Name
Wave Height	Capacitance Wave Gauge	SG2000 (Basin)	0-0.6 m	±1 mm	50 Hz
	Capacitive Wave Probe	— (Large Flume)	0-5 m	1% F.S.	50 Hz
Six-DOF Motion	Optical Motion Capture System	Nokov-Mars	52°×52°	±0.1 mm	100 Hz
Mooring Line Force	Submersible Tension Load Cell	LA2-type	50-100 N	0.05% F.S.	1000 Hz
Flow Velocity	Acoustic Doppler Velocimeter (ADV)	Vectrino+	0-3 m/s	±1%±0.5 cm/s	100 Hz
Wind Speed	Hot-Wire Anemometer	-	0-10 m/s	±0.1 m/s	50 Hz
Wind/Current Drag Force	Three-Component Force Sensor	-	0-100 N	0.15% F.S.	100 Hz

(1) Wave Measurement System: Wave height measurement formed the foundation of the tests. Capacitive wave probes and capacitance wave gauges were employed in the large flume and the basin, respectively. All sensors underwent rigorous calibration prior to testing, exhibiting a linearity greater than 0.999.

(2) Motion Measurement System: The six-degree-of-freedom (6-DOF) motions of the buoy were measured using a Nokov-Mars series optical motion capture system via a non-contact method. This system tracks multiple infrared reflective markers fixed on the buoy model. Through dedicated post-processing software, it directly outputs time-history data of displacement and rotation at the buoy's center of gravity. This approach avoids the added mass effect associated with contact sensors and offers high precision and strong anti-interference capability.

(3) Force Measurement System: Mooring line tension was measured using a high-precision, waterproofed submersible tension load cell, connected in series directly between the mooring chain

 doi:10.20944/preprints202605.0930.v1

and the buoy base. Environmental loads from wind and current were measured integrally using a three-component force sensor mounted on a dedicated frame.

(4) Data Acquisition System: Signals from all sensors were acquired by a multi-channel synchronous data acquisition unit. The sampling frequency was set between 50 Hz and 1000 Hz depending on the characteristics of the physical quantity being measured, ensuring the capture of high-frequency dynamic responses. The entire data acquisition process was controlled by a central computer, guaranteeing strict synchronization of timestamps across all systems.

2.2.3. Test Methods

(1) Free Decay Test: Under calm water conditions, an initial displacement was applied to the buoy model and then released, allowing it to oscillate freely. The optical motion capture system was used to record the decay time-history curves of the roll and heave motions. The non-dimensional damping coefficient ζ was calculated using Equation (6), and the average value from three repeated tests was taken as the final result.

$$\eta = \frac{1}{\pi(N-1)} \sum_{i=2}^{N} \left(ln \left| \frac{\eta_{i-1}}{\eta_i} \right| \right), \quad |\eta_{i-1}| > |\eta_i| \tag{6}$$

where η_i, η_{i-1} represent the amplitudes of the i and $i-1$ oscillation peaks, respectively.

(2) Motion RAO Measurement: Under regular wave action, the motion response of the buoy model is measured after it reaches a steady state. The Response Amplitude Operator (RAO) is calculated according to Equation (7).

$$Y_A(\omega) = \frac{y_A(\omega)}{\xi_A} \tag{7}$$

Each regular wave condition is repeated three times, and the average motion amplitude is used for calculation to eliminate random errors.

(3) Wind/Current Drag Coefficient Determination: In a uniform flow or wind field, the total drag force F acting on the buoy model is measured. The wind drag coefficient C_D and current drag coefficient C_C are calculated using Equations (8) and (9), respectively.

$$F_W = \frac{1}{2} \rho C_D U^2 A \tag{8}$$

$$F_C = \frac{1}{2} \rho C_C V^2 A \tag{9}$$

where ρ denotes the fluid density (ρ_a = 1.2 kg/m³ for air and ρ_w = 1.0 × 10³ kg/m³ for seawater), C_D is the wind drag coefficient, C_C is the current drag coefficient, U is the wind speed, V^2 is the current velocity, and A represents the projected area normal to the wind or current direction. The projected areas for wind and current are taken as 18.955 m² and 9.075 m², respectively.

(4) Statistical Analysis Method: For irregular wave tests, the measured motion and force time-history data are subjected to statistical analysis to derive characteristic statistical quantities, including the mean, significant value, 1/10 maximum value, and 1/100 maximum value. All data analyses are processed using professional software to ensure the scientific rigor and accuracy of the results.

2.2.4. Discussion on Scale Effects

The present model tests were conducted primarily following the Froude similarity criterion to accurately reproduce gravity-dominated wave dynamic processes. The similarity criteria and data analysis methods employed in the model tests were referenced from relevant offshore engineering standards [34,35]. However, in the determination of wind and current drag coefficients, the flow around the object and its drag characteristics are influenced by both gravitational and viscous forces simultaneously, requiring similarity in both Froude number (*Fr*) and Reynolds number (*Re*). Under

 doi:10.20944/preprints202605.0930.v1

a fixed geometric scale of λ = 10, satisfying *Fr* similarity necessitates scaling the model velocity according to $\lambda_V = \lambda^{1/2}$, whereas satisfying *Re* similarity requires scaling according to $\lambda_V = \lambda^{-1}$; these two requirements are mutually contradictory. Therefore, the scale effect arising from Reynolds number dissimilarity constitutes an inherent theoretical limitation within the present experimental framework.

To evaluate and minimize the influence of scale effects on drag coefficient measurements, the following measures were adopted in this study:

(1) Ensuring surface roughness similarity: The surface finish of the model buoy was maintained consistent with that of the prototype to control the boundary layer transition point, thereby ensuring that the model operates in a flow regime as similar as possible to that of the prototype (turbulent flow regime).

(2) Increasing experimental Reynolds number: By employing a large-scale model (1:10) and selecting relatively high wind and current velocity conditions for testing, the model Reynolds number (Re_m) was ensured to enter the "self-similarity region" (i.e., the range where the drag coefficient becomes insensitive to variations in *Re*). It is estimated that the Reynolds number range in the present tests (based on the disc diameter as the characteristic length) is approximately 2×10^5 to 1×10^6 (for current) and 1×10^5 to 5×10^5 (for wind), which has essentially reached or exceeded the critical Reynolds number, resulting in a relatively stable flow separation point.

(3) Focusing on coefficient trends rather than absolute values: The experimental results (see Section 4.4) indicate that within the tested wind and current velocity ranges, the drag coefficients remain relatively stable without significant fluctuations, suggesting to a certain extent that the influence of scale effects within the present test parameter range is controllable.

In summary, although complete elimination of scale effects in physical model testing presents considerable challenges, the drag coefficients measured in this study ($C_D \approx 0.76$, $C_C \approx 0.44$) are capable of effectively reflecting the load characteristics of this buoy type within the corresponding Reynolds number ranges, thereby providing critical and reliable input parameters for engineering design. Caution should be exercised when extrapolating these results to the prototype, noting that they are based on the Froude similarity framework.

2.2.5. Coordinate System Definition and Experimental Setup

(1)Coordinate System Definition

To accurately describe the motion response of the buoy in waves, a right-handed Cartesian coordinate system is established as illustrated in Figure 1. The origin O is defined at the center of the buoy's base plane in its static equilibrium position. The positive X-axis points toward the bow of the buoy (incident flow direction), the positive Y-axis is perpendicular to the X-axis and points toward the port side, and the Z-axis is directed vertically upward in accordance with the right-hand rule. The wave incidence angle β is defined as the angle between the wave propagation direction and the positive X-axis, with 0° along the positive X-axis and positive angles measured counterclockwise.

The six-degree-of-freedom (6-DOF) motions of the buoy are defined as follows: translation along the OX axis—surge; translation along the OY axis—sway; translation along the OZ axis—heave; rotation about the OX axis—roll; rotation about the OY axis—pitch; and rotation about the OZ axis—yaw.

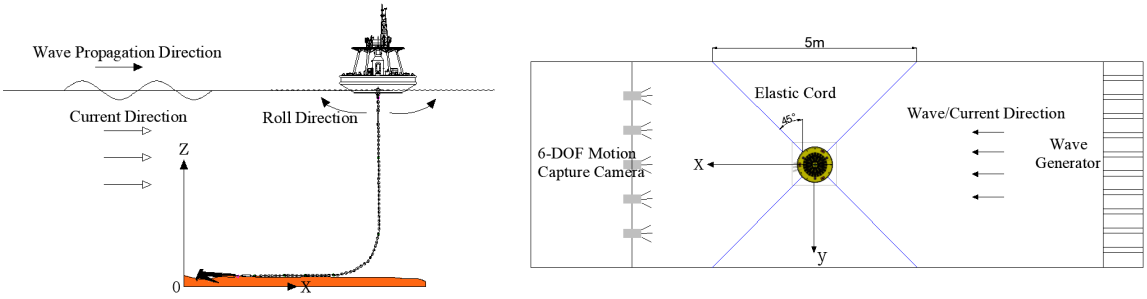

 doi:10.20944/preprints202605.0930.v1

(**a**) (**b**)

Figure 1. Schematic of the coordinate system and definition of the wave incidence angle.

(2) Experimental Setup

A single-point mooring configuration was adopted in the experiment, with the mooring chain attachment point located at the center of the buoy bottom. The model arrangement strictly adhered to the similarity criteria, and the setups in the two test facilities are schematically illustrated in Figure 2.

In the large-scale wave flume, the model was positioned approximately 200 m from the wavemaker to ensure full wave development. To minimize boundary effects, the distance from the model center to each side wall was maintained at more than twice the model diameter. In the harbor and coastal engineering basin, the model was placed approximately 30 m from the wavemaker, with the distance to both side boundaries exceeding 1.5 times the model diameter.

The measurement systems were arranged as follows:

① Wave gauges were installed at 2 m, 5 m, and 8 m upstream of the model to monitor the free surface elevation time history and wave height distribution;

② Optical motion capture cameras were positioned directly above and at the rear side of the model to ensure complete acquisition of the six-degree-of-freedom motions;

③ A submersible tension load cell was connected in series between the mooring chain and the buoy attachment point to measure the dynamic response of the mooring line;

④ Current meters and anemometers were placed at a distance of twice the model diameter upstream of the model in the incident flow direction to avoid flow interference.

(**a**) (**b**)

Figure 2. Schematic of the experimental setup: (a) in the large-scale wave flume; (b) in the harbor basin.

2.2.6. Test Condition Design

Based on the actual operational sea states of the buoy, four major categories of test conditions were designed in this study, with a total of 158 effective test runs conducted, as summarized in Table 4.

Table 4. Summary of the test conditions.

Test Type	Test Conditions	Number of Runs	Test Type	Test Conditions
Calm-water decay	Without mooring chain / With mooring chain	12	Roll and heave decay curves	Large flume
	Period2.5-15 s	108		

 doi:10.20944/preprints202605.0930.v1

Regular wave RAO	Wave direction 0°-180°		Six-DOF motion, Wave surface	Both facilities
Irregular wave	Moderate sea state: H_s=2.0 m Extreme sea state: H_s=13.8 m	18	Motion response, Mooring line tension time histories	Large flume
Environmental load	Wind speed20-60 m/s Current velocity2-6knot	20	Wind/current drag force, Wave surface Six-DOF motion, Wave surface	Harbor basin

The test procedures for each condition are described as follows:

① Calm-water decay test: Initial displacements were applied to the model in the roll and heave directions, respectively, and then released to record the free decay curves. Each group was repeated three times.

② Regular wave test: The wave height was controlled within H/λ = 1/35–1/50, covering prototype periods of 2.5–15 s. Each period condition was repeated three times.

③ Irregular wave test: The JONSWAP spectrum (γ = 3.3) was adopted, with at least three random seed numbers and a duration of no less than 3 hours (prototype time).

④ Environmental load test: Wind speed and current velocity were increased in gradients, with a stable measurement duration of no less than 3 minutes (prototype time) for each condition.

All tests followed the following quality control standards: wave height repeatability error: ±3%; motion measurement error: ±0.5°; force measurement error: ±0.5% F.S.; data sampling frequency: 50 Hz (motion), 100 Hz (force); minimum number of repetitions per group: 3.

3. Results and Discussions

3.1. Natural Characteristics and Damping Identification of the Buoy

The free decay motion of a floating body in calm water is a direct manifestation of its inherent dynamic characteristics, which is crucial for predicting its motion response in waves [1]. In this study, the natural period and damping characteristics of the novel 10-m disk-shaped buoy were accurately identified through calm-water decay tests, with the results presented in Table 5. With the advancement of GNSS technology, novel real-time wave measurement buoys have provided more options for ocean observation [36].

Table 5. Results of the free-decay tests in calm water.

Motion Mode	Buoy Condition	Natural Period T (s)	Non-dimensional Damping Ratioζ	Motion Mode
Roll	Without mooring chain	3.05	0.15	Average of three repeated tests
	With mooring chain	2.92	0.14	Average of three repeated tests
Heave	Without mooring chain	3.65	-	-
	With mooring chain	3.53	-	-

The analysis indicates that the mooring system has a limited influence on the natural characteristics of the buoy. The natural roll periods without and with the mooring chain are 3.05 s and 2.92 s, respectively, with a deviation of approximately 4.3%; the natural heave periods are 3.65 s and 3.53 s, respectively, with a deviation of approximately 3.3%. This phenomenon can be explained

 doi:10.20944/preprints202605.0930.v1

from a dynamic perspective: under this single-point mooring arrangement, the mooring chain primarily provides restoring force to restrict the drift of the buoy, while exerting weak constraint on the rotation about the center of gravity (roll) and vertical motion (heave) of the floating body; therefore, its natural frequency is mainly determined by the mass moment of inertia and hydrodynamic stiffness of the buoy itself.

The non-dimensional roll damping ratio ζ of this disk-shaped buoy was measured as 0.14 (with mooring chain) and 0.15 (without mooring chain), as presented in Table 5, indicating a narrow range of 0.14–0.15 across test conditions. This value is significantly higher than that of traditional ship-type buoys (typically $\zeta < 0.1$) [37,38] and most cylindrical (Spar-type) buoys (typical range 0.08-0.12) [35,39]. This significant difference in damping characteristics originates from the unique hull form design and the induced hydrodynamic mechanism.

From a hydrodynamic perspective, this buoy features a large beam-to-draft ratio (D/T ≈ 10), shallow draft, and an approximately flat-bottom geometry. When roll motion occurs, the underwater volume distribution changes dramatically with heel angle, resulting in significant transverse motion of the hull near the waterline. This motion efficiently generates radiated waves, thereby rapidly converting the system's mechanical energy into propagating wave energy that dissipates into the far field—this is the primary contribution of radiation damping [40]. For disk-shaped blunt bodies, radiation damping often dominates the total roll damping, with an efficiency that far exceeds that of slender hull forms that primarily rely on bilge keel friction and vortex shedding [41]. Additionally, the sharp-edged geometry may promote flow separation during rolling, generating additional viscous damping.

This inherent high-damping characteristic endows this buoy type with distinct engineering advantages:

(1) Amplitude suppression of motion response: Under high damping, the peak value of the motion response amplitude operator (RAO) near the resonant frequency (approximately 3.0 s in this test) is effectively suppressed. Although a significant resonance peak is still observable, its amplitude is substantially reduced by energy dissipation, directly enhancing the motion stability of the buoy under common sea states.

(2) Rapid attenuation of motion: High damping implies faster free decay of the system. When the buoy is subjected to transient impacts (such as breaking wave impacts) or intermittent large wave groups, its residual oscillation attenuates more rapidly, facilitating quick recovery to a stable attitude—this is essential for ensuring continuous normal operation of onboard instruments (such as radars, communication antennas, and optical sensors).

(3) Mitigation of mooring dynamic loads: The amplitude and acceleration of roll motion are important factors driving the dynamic tension of the mooring system. Higher damping helps to limit motion amplitude and smooth the motion time history, thereby reducing the dynamic amplification factor and fatigue load spectrum of the mooring line tension, thereby improving the long-term reliability and service life of the mooring system.

Therefore, the high roll damping revealed in this study is not merely a characteristic parameter of this disk-shaped buoy, but a key advantage in its seakeeping design. It enables this buoy type to possess potential performance benefits when facing monitoring tasks with stringent platform stability requirements (such as high-precision meteorological observation, optical remote sensing, and communication relay), providing important hydrodynamic basis for buoy selection and optimization design.

Furthermore, a noteworthy refinement was observed during the tests: compared with the free state without mooring chain, the presence of the mooring chain, although having limited influence on the natural periods of roll and heave (variation < 5%), slightly increases the overall system damping (see Table 5). This phenomenon can be explained from the perspective of chain-water interaction: the relative motion between the mooring chain and the surrounding water generates additional viscous damping, thereby slightly enhancing the total energy dissipation capability of the system. Although this increment is relatively small compared with the radiation damping of the buoy

 doi:10.20944/preprints202605.0930.v1

itself, it reveals the existence of subtle coupling effects between the mooring system and the dynamic response of the floating body.

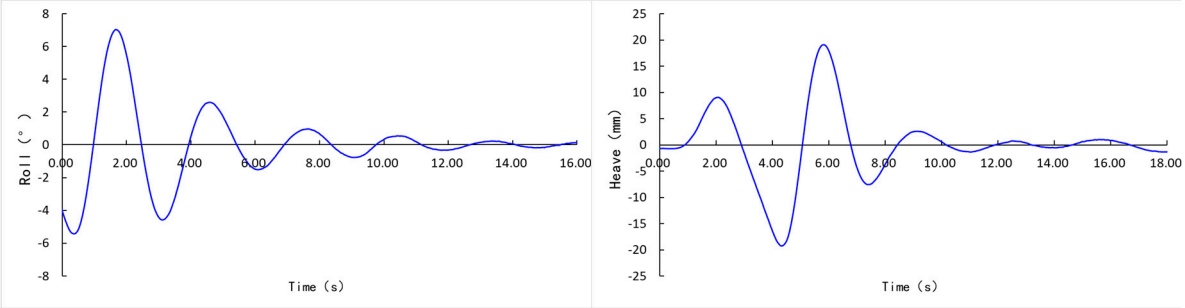

(**a**) (**b**)

Figure 3. Typical free-decay time histories of the moored buoy in calm water: (a) roll; (b) heave.

In summary, this study has identified not only the high damping characteristics determined by the hull form itself, but also the marginal enhancement effect of the mooring system on the total damping. These accurately measured dynamic parameters (natural period, damping ratio) through experiments collectively constitute a complete description of the dynamic behavior of this buoy system, serving as indispensable fundamental data for subsequent accurate prediction of its motion response in waves and for calibration and validation of related numerical simulation models.

3.2. Analysis of Motion Response Characteristics in Regular Waves

The Response Amplitude Operator (RAO) is a core indicator for characterizing the linear motion performance and evaluating the seakeeping behavior of floating bodies, and it is of great significance for predicting motion in random waves [1]. Through systematic regular wave tests, this study obtained the RAOs of the buoy in the two principal degrees of freedom (roll and heave), profoundly revealing the laws governing its motion response. Research on variable-shape buoy wave energy converters has shown that the hydrodynamic performance and energy capture efficiency can be significantly optimized through actively adjusting the buoy geometry [42].

The motion responses of the buoy under regular waves of different periods were systematically measured in both moored and free-floating conditions, and the corresponding RAO values were calculated accordingly. The detailed data are presented in Table 6. The analysis results demonstrate that the motion response characteristics of the buoy exhibit significant frequency dependence and degree-of-freedom differentiation.

Table 6. Characteristic RAO values of the buoy under regular waves.

Motion Mode	Buoy Condition	RAO Peak Value	Wave Period(s)	RAO (T=15s)
Roll(°/m)	Without mooring chain	25.98	3.00	1.10
	With mooring chain	26.60	3.00	1.42
Heave(m/m)	Without mooring chain	1.04	11.00	1.01
	With mooring chain	1.00	5.90	0.89

The roll motion response exhibits violent resonance near the wave period of 3.00 s, with RAO peak values reaching 25.98°/m and 26.60°/m for the conditions without and with mooring chain, respectively. This peak period is in excellent agreement with the natural roll period of the buoy measured in Section 4.1 (approximately 3.0 s), indicating that resonance occurs when the wave excitation frequency coincides with the natural frequency of the floating body, resulting in drastic amplification of the motion response. In engineering practice, this dangerous period must be strictly avoided to prevent structural fatigue or equipment failure caused by resonance. Outside the resonance region (T > 5 s), the roll RAO decays rapidly with increasing period. Similarly, Shi et al. [43] investigated a mass-adjustable buoy-type wind-wave energy converter and found that the RAO

 doi:10.20944/preprints202605.0930.v1

curve of the buoy in regular waves also exhibits pronounced resonance peak characteristics, and the dynamic response can be effectively controlled through mass adjustment.

The heave motion response exhibits characteristics different from those of roll. Its RAO curve is relatively flat, with a peak RAO of 1.04 at the period of 11.0 s for the free-floating condition and an RAO of 1.00 at the period of 5.9 s for the moored condition. In the long-period range (T > 10 s), the heave RAO approaches 1.0, indicating that the floating body enters the wave-following regime wherein its motion synchronizes with the wave surface. As shown in Figure 4b, the heave RAO is plotted as a function of wave period (x-axis: wave period T in seconds, y-axis: heave RAO in m/m). The data points for the free-floating and moored conditions are distinguished by open circles and filled squares, respectively; the solid lines represent spline fits to the experimental data. Error bars based on three repeated tests are shown for each data point, indicating good repeatability with a coefficient of variation generally below 5%. Comparison of the RAO curves with and without mooring chain reveals that both curves are very similar in shape and magnitude throughout the entire test period range. This confirms that, under this single-point mooring arrangement, the angular and vertical motions of the buoy are primarily determined by its own hydrodynamic geometry and mass distribution, while the main function of the mooring system is to restrain its horizontal drift.

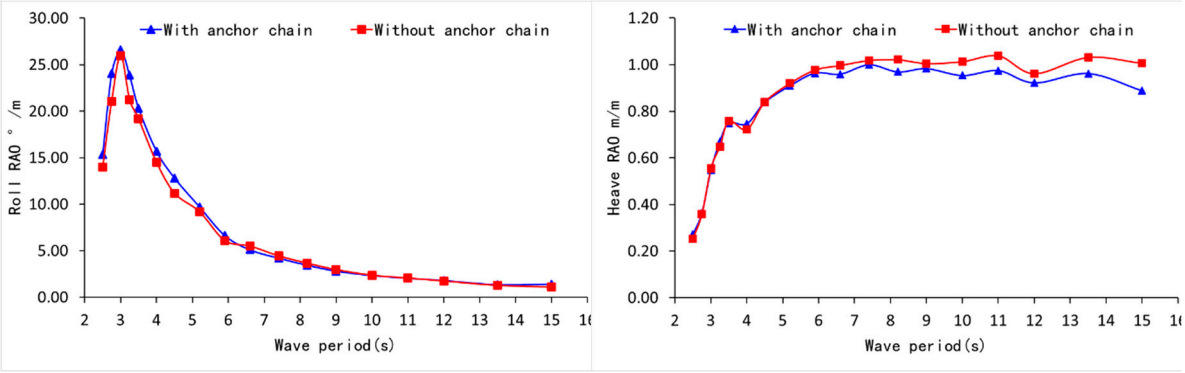

(**a**) (**b**)

Figure 4. Motion RAOs of the buoy under regular waves: (a) roll; (b) heave.

3.3. Analysis of Motion and Mooring Line Tension Response under Extreme Sea States

The survival capability of a buoy under extreme sea states is a core criterion for its design evaluation. This study tested the motion and mooring line tension responses of the moored buoy under extreme sea states (H_s = 13.8 m, T_p = 16.1 s) and moderate sea states (H_s = 2.0 m, T_p = 8.5 s), aiming to assess its safety performance. The key statistical results are presented in Table 7.

Table 7. Comparison of the buoy's characteristic response values under extreme and moderate sea states (prototype scale).

Sea State	Significant Roll (°)	Maximum Roll (°)	Significant Heave (m)	Maximum Heave (m)	Significant Tension (kN)
Extreme sea state	12.82	21.30	6.41	8.96	61.56
Moderate sea state	5.46	7.82	0.96	1.42	24.81

The motion and mooring response of the buoy under extreme sea states constitute important indicators of its survival capability. According to the test results, under the action of the extreme sea state (H_s = 13.8 m, T_p = 16.1 s), the buoy exhibited significant motion responses. The significant roll reached 12.82°, with a maximum roll angle of 21.30°; the significant heave was 6.41 m, with a maximum heave amplitude of 8.96 m. These data indicate that the buoy underwent severe motion responses under extreme sea states.

 doi:10.20944/preprints202605.0930.v1

The mooring line tension test results reveal that, under extreme sea states, the dynamic response of the line tension was pronounced. The initial pretension was 20.5 kN, while the maximum dynamic tension reached 61.56 kN, approximately 3.0 times the initial pretension. This significant dynamic amplification effect indicates that the influence of dynamic loads must be considered in the design of the mooring system. The maximum line tensions measured in three repeated tests ranged from 48.55 kN to 61.56 kN, demonstrating the reproducibility of the test results.

Figure 5 presents the time histories of the buoy motion and mooring line tension under the extreme sea state (H_s = 13.8 m, T_p = 16.1 s). All four subplots share a common x-axis representing prototype time in seconds (0–1200 s). Subplot (a) shows the incident wave elevation (y-axis in metres) measured by the capacitance wave gauge; subplot (b) shows the heave response (y-axis in metres); subplot (c) shows the roll response (y-axis in degrees); and subplot (d) shows the mooring line tension (y-axis in kilonewtons), with the horizontal dashed line indicating the initial static pretension of 20.5 kN for reference.

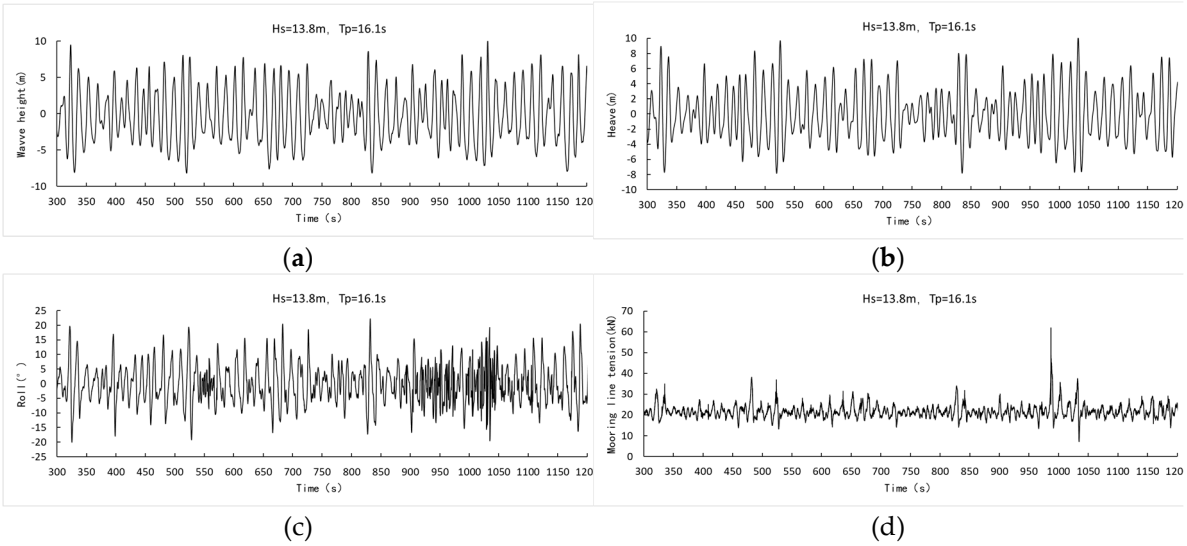

Figure 5. Time histories of buoy motion and mooring line tension under extreme sea state: (a) wave height; (b) heave; (c) roll; (d) mooring line tension.

Comparison with the test results under moderate sea states (H_s = 2.0 m, T_p = 8.5 s) reveals that both motion responses and line tension values increased significantly under extreme sea states. The significant roll increased from 5.5° to 12.8°, the significant heave increased from 0.96 m to 6.41 m, and the maximum line tension increased from 24.81 kN to 61.56 kN. This order-of-magnitude change highlights the pronounced influence of sea state conditions on buoy performance.

The test results demonstrate that this buoy type can maintain structural integrity under extreme sea states without exhibiting capsizing tendencies. However, the dynamic loads borne by the mooring system far exceed the static pretension, which requires particular attention in subsequent mooring system design. It is recommended that the dynamic load extremes measured in this study be employed for mooring chain selection and strength verification, ensuring that the mooring system possesses adequate safety margins. Yu et al. [44] investigated single-point mooring systems for buoys and demonstrated that the elastic deformation characteristics of electro-optical-mechanical cables exert significant restraining effects on the horizontal-plane motions of buoys, with their design approach providing valuable reference for engineering applications of similar buoy mooring systems.

3.4. Analysis of Wind and Current Load Characteristics

Accurate determination of wind drag coefficient and current drag coefficient is of significant importance for the mooring system design, motion response prediction, and positioning accuracy

 doi:10.20944/preprints202605.0930.v1

evaluation of floating bodies. Through wind tunnel tests and flume experiments, this study systematically determined the wind and current load characteristics of this novel 10-m disk-shaped buoy, with the results presented in Table 8.

Table 8. Experimental results of the wind and current drag coefficients.

Load Type	Test Run	Prototype Environmental Parameter	Measured Load (kN)	Drag Coefficient
Wind load	1	10.44 m/s (20.28 knots)	1.35	0.74
	2	13.41 m/s (26.06 knots)	2.33	0.77
	3	21.25 m/s (41.31 knots)	5.64	0.74
	4	25.77 m/s (50.10 knots)	8.39	0.75
	5	33.20 m/s (64.54 knots)	14.67	0.79
Current load	1	1.03 m/s (2.00 knots)	1.96	0.39
	2	2.06 m/s (4.24 knots)	9.86	0.46
	3	3.09 m/s (6.00 knots)	19.84	0.46

The analysis results indicate that, within the tested current velocity range (2–6 knots), the current drag coefficient C_C ranges between 0.39 and 0.46, with an average value of 0.44 (Figure 6a). Its value remains relatively stable, indicating that no significant change in flow separation point occurred within this velocity interval. In Figure 6a, the current drag coefficient C_C, current is plotted against current velocity (x-axis: current speed in knots, y-axis: drag coefficient), with data points denoted by filled diamonds and the horizontal solid line representing the mean value of 0.44. Within the tested wind speed range (20.28–64.54 knots), the wind drag coefficient C_D ranges between 0.74 and 0.79, with an average value of 0.76 (Figure 6b). In Figure 6b, the wind drag coefficient C_D, wind is plotted against wind speed (x-axis: wind speed in knots, y-axis: drag coefficient), with data points denoted by open triangles and the horizontal solid line representing the mean value of 0.76. This value falls within the empirical range for disk-type floating bodies of this class, and exhibits a slightly increasing trend with increasing wind speed, which may be related to changes in flow structure at different Reynolds numbers.

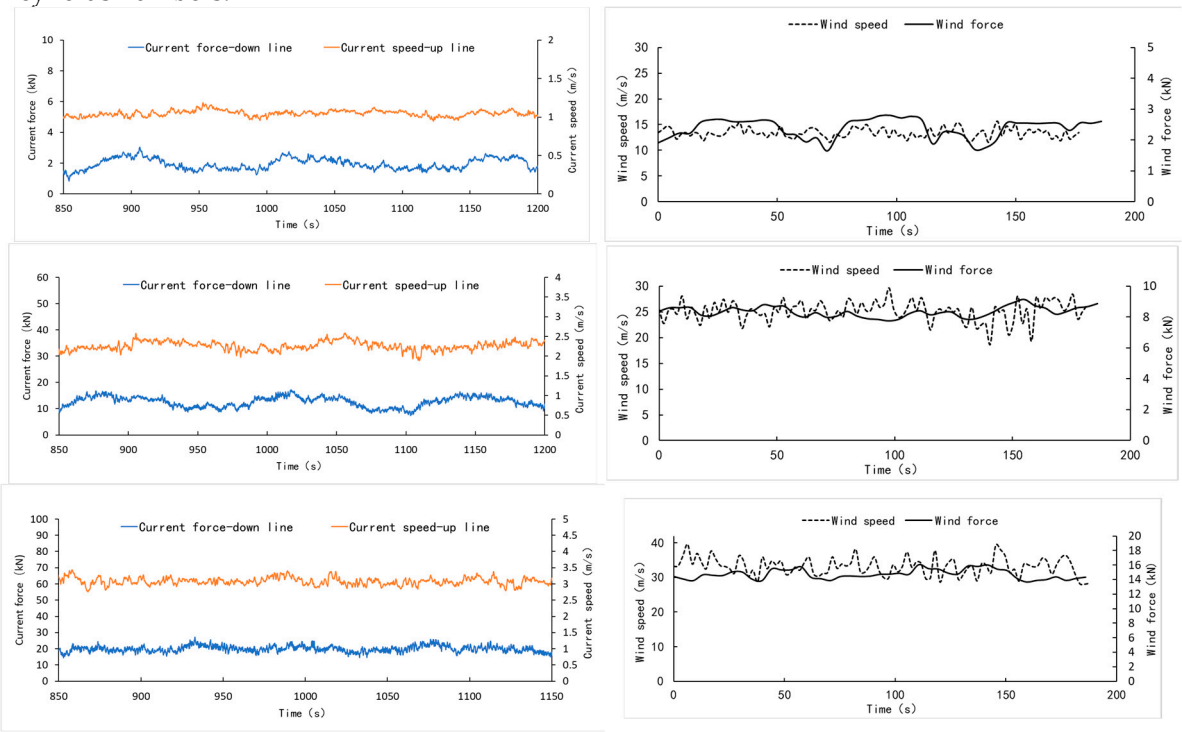

(a) (b)

Figure 6. Experimental results of the drag coefficients: (a) current drag coefficient; (b) wind drag coefficient.

 doi:10.20944/preprints202605.0930.v1

The drag coefficients measured in this study provide critical parameters for the accurate design of this buoy and its mooring system. The wind drag coefficient can be employed to calculate wind-induced drift force and its contribution to capsizing moment, while the current drag coefficient serves as a core input for predicting buoy offset in tidal currents and calculating mooring system restoring force. These measured data effectively avoid design deviations resulting from the adoption of empirical coefficients, significantly enhancing the economy and safety of engineering design.

4. Conclusions

Through systematic physical model tests, this study conducted an in-depth investigation into the hydrodynamic performance of a novel 10-m disk-shaped buoy under combined wind, wave, and current actions. The following main conclusions are drawn:

(1) In terms of buoy dynamic characteristics, the inherent dynamic parameters of the buoy were accurately identified through calm-water decay tests. The natural roll period of the buoy is approximately 3.0 s, the natural heave period is approximately 3.6 s, and the non-dimensional roll damping ratio is 0.14–0.15. The tests demonstrate that the mooring system has limited influence on these natural characteristics, which are primarily determined by the mass distribution and hydrodynamic geometry of the buoy itself. The relatively high roll damping ($\zeta \approx 0.14$–0.15) constitutes a significant advantage of this buoy type, contributing to enhanced motion stability and operational reliability of onboard instruments.

(2) In terms of motion response laws, the regular wave tests reveal pronounced characteristics of the buoy motion. Violent resonance occurs in roll motion near the wave period of 3.0 s, with RAO peak values exceeding 26°/m, which is in excellent agreement with the natural period; this dangerous period must be strictly avoided in actual operations. The heave motion exhibits favorable wave-following regime for periods greater than 5 s, with RAO values approaching 1.0.

(3) In terms of extreme sea state performance, the test results indicate that the buoy possesses favorable survival capability. Under extreme sea states (H_s = 13.8m, T_p = 16.1s), the maximum roll angle is 21.30° and the maximum heave amplitude is 8.96 m, with no tendency toward capsizing observed. The mooring system exhibits a significant dynamic amplification effect, with the maximum dynamic line tension reaching 61.56 kN, approximately 3.0 times the initial pretension; this dynamic factor serves as the controlling basis for mooring system strength design.

(4) In terms of environmental load characteristics, accurate load design parameters were obtained through tests. The mean wind drag coefficient of the buoy is 0.76, and the mean current drag coefficient is 0.44, filling the data gap for load coefficients of this type of floating body and providing reliable input for precise load calculation in engineering design.

This study not only provides complete data support and theoretical basis for the design optimization and safe operation of this specific buoy, but its systematic experimental methodology, comprehensive database, and in-depth understanding of dynamic characteristics also offer valuable reference for the research and development of similar ocean buoys. It is recommended that subsequent research focus on the nonlinear dynamic optimization of mooring systems to further enhance the survival capability of buoys under extreme sea states, and conduct comprehensive uncertainty analyses to quantify the effects of measurement errors, scaling effects, and statistical variability on the reliability of experimental results.

Author Contributions: Conceptualization, Z.T., H.C., S.C. and N.G.; methodology, Z.T., H.C., S.C. and N.G.; software, Z.T.; validation, S.C., N.G. and H.C.; formal analysis, Z.T. and S.C.; investigation, Z.T., Y.L. and W.S.; resources, H.C. and W.S.; data curation, Z.T. and Y.L.; writing—original draft preparation, Z.T.; writing—review and editing, S.C., N.G., H.C., Y.L. and W.S.; visualization, Z.T.; supervision, H.C., S.C. and N.G.; project administration, H.C.; funding acquisition, H.C. and N.G. All authors have read and agreed to the published version of the manuscript.

Funding: This work was financially supported by the National Key Research and Development Program of China (2025YFE0117200), the Basic Funding of the 566 Central Public Research Institute (TKS20260201).

 doi:10.20944/preprints202605.0930.v1

Institutional Review Board Statement: No applicable.

Informed Consent Statement: No applicable.

Data Availability Statement: The data presented in this study are available upon reasonable request from the corresponding author. Restrictions apply to the availability of raw test data due to institutional policy.

Acknowledgments: The authors gratefully acknowledge the technical support provided by the engineering staff of the Tianjin Research Institute for Water Transport Engineering (TIWTE) for the large-scale wave flume and harbor basin experiments. Special thanks are extended to the technicians for their assistance in model fabrication, instrument calibration, and data acquisition. The authors have reviewed and edited the output and take full responsibility for the content of this publication. The authors also thank the anonymous reviewers for their constructive comments, which helped improve the quality of this manuscript.

Conflicts of Interest: The authors declare no conflicts of interest. The funders had no role in the design of the study; in the collection, analyses, or interpretation of data; in the writing of the manuscript; or in the decision to publish the results.

References

1. Yu, J.X.; Han, T.; Li, L.Q.; et al. Research status analysis of hydrodynamic characteristics of marine data buoys. Trans. Oceanol. Limnol. 2017, 4, 7–15.
2. Liu, T.J.; Li, X.; Zhang, Y.Q.; et al. Hydrodynamic performance test of double-floating wave power buoy. J. Sol. Energy 2017, 38, 1078–1084.
3. Xu, R.; Wang, H.; Xi, Z.; Wang, W.; Xu, M. Recent Progress on Wave Energy Marine Buoys. J. Mar. Sci. Eng. 2022, 10 (5), 566. https://doi.org/10.3390/jmse10050566
4. Zheng, X.Q.; Zhu, K.Q.; Zhang, D.P.; et al. Hydrodynamic analysis of the single point mooring metocean buoy in deep water. J. Waterw. Harb. 2018, 39, 96–100. https://doi.org/10.3969/j.issn.1005-8443.2018.01.017
5. Newman, J.N. Marine Hydrodynamics; MIT Press: Cambridge, MA, USA, 1977.
6. Thiagarajan, K.P.; Troesch, A.W. Effects of appendages and small currents on the hydrodynamic heave damping of TLP columns. ournal of Offshore Mechanics & Arctic Engineering 120.1(1996):37-42.
7. Lloyd, A.R.J.M. Seakeeping: Ship Behaviour in Rough Weather; ARJMLloyd: Gosport, UK, 1989.
8. Ryu, S.; Duggal, A.S.; Heyl, C.N.; et al. Coupled analysis of deepwater oil offloading buoy and experimental verification. In Proceedings of the 15th International Offshore and Polar Engineering Conference, Seoul, Korea, 19–24 June 2005; ISOPE-I-05-022.
9. Ryu, S.; Duggal, A.S.; Heyl, C.N.; Liu, Y. Prediction of deepwater oil offloading buoy response and experimental validation. Int. J. Offshore Polar Eng. 2006, 16, 290–296.
10. Le Cunff, C.; Ryu, S.; Duggal, A.; et al. Derivation of CALM buoy coupled motion RAOs in frequency domain and experimental validation. In Proceedings of the 17th International Offshore and Polar Engineering Conference, Lisbon, Portugal, 1–6 July 2007; ISOPE-I-07-402.
11. Salem, A.G.; Ryu, S.; Duggal, A.S.; Datla, R.V. Linearization of quadratic drag to estimate CALM buoy pitch motion in frequency-domain. In Proceedings of the 28th International Conference on Ocean, Offshore and Arctic Engineering, Honolulu, HI, USA, 31 May–5 June 2009. https://doi.org/10.1115/OMAE2009-80212
12. Jeong, S.-M.; Son, B.-H.; Lee, C.-Y. Estimation of the Motion Performance of a Light Buoy Adopting Ecofriendly and Lightweight Materials in Waves. J. Mar. Sci. Eng. 2020, 8 (2), 139. https://doi.org/10.3390/jmse8020139
13. Lu, K.; Rao, X.; Wang, H.M.; et al. The influences of different mooring systems on the hydrodynamic performance of buoy. Acta Armamentarii 2022, 43, 120–130. https://doi.org/10.3969/j.issn.1000-1093.2022.01.013
14. Zhu, L.; Hu, J.P. Analysis and optimization of wave-following performance of wave observation buoy based on AQWA. Guangdong Shipbuild. 2018, 37, 50–54, 63. https://doi.org/10.3969/j.issn.2095-6622.2018.02.014

 doi:10.20944/preprints202605.0930.v1

15. Chang, Z.Y.; Wang, L.; Gao, D.X.; et al. Dynamic analysis of single-point moored surface buoy during deployment process. China Sci. Pap. Online 2011. Available online: http://www.paper.edu.cn/releasepaper/content/201105-18 (accessed on 3 May 2011).
16. Li, Y.; Yang, F.; Li, S.; Tang, X.; Sun, X.; Qi, S.; Gao, Z. Influence of Six-Degree-of-Freedom Motion of a Large Marine Data Buoy on Wind Speed Monitoring Accuracy. J. Mar. Sci. Eng. 2023, 11 (10), 1985. https://doi.org/10.3390/jmse11101985
17. Hegde, C.; Nallayarasu, S. Hydrodynamic response of buoy form spar with heave plate near the free surface validated with experiments. Ocean Eng. 2023, 269, 113580. https://doi.org/10.1016/j.oceaneng.2022.113580
18. Zhu, L.; Lim, H.-C. Hydrodynamic characteristics of a separated heave plate mounted at a vertical circular cylinder. Ocean Eng. 2017, 131, 213–223. https://doi.org/10.1016/j.oceaneng.2017.02.032
19. Capobianco, R.; Rey, V.; Calvé, O.L. Experimental survey of the hydrodynamic performance of a small spar buoy. Appl. Ocean Res. 2002, 24, 309–320. https://doi.org/10.1016/S0141-1187(03)00026-9
20. Tao, L.; Dray, D. Hydrodynamic performance of solid and porous heave plates. Ocean Eng. 2008, 35, 1006–1014. https://doi.org/10.1016/j.oceaneng.2008.03.003
21. Wang, H.M.; Lu, K.; Liang, S.G. Experimental study on hydrodynamic influence of marine data buoy with different mooring systems in Northern Part of Weihai. In Proceedings of the International Conference on Advances in Engineering Technology, Madison, WI, USA, 7-9 August 2023. https://doi.org/10.56028/aetr.7.1.255.2023.
22. Cao, H.Y. Study on the Resistance and Motion Characteristics of A Marine Pillar Buoy. Master's Thesis, Tianjin University, Tianjin, China, 2012. DOI:10.7666/d.D323187.
23. Zhang, J.M.; Fan, X.T.; Zhao, Q.; et al. Simulation study on hydrodynamic characteristics of marine data buoy in frequency domain. Shandong Sci. 2015, 28, 8–13. https://doi.org/10.3976/j.issn.1002-4026.2015.04.002
24. Eriksson, M.; Isberg, J.; Leijon, M. Hydrodynamic modelling of a direct drive wave energy converter. Int. J. Eng. Sci. 2005, 43, 1377–1387. https://doi.org/10.1016/j.ijengsci.2005.05.014
25. Eriksson, M.; Isberg, J.; Leijon, M. Theory and experiment on an elastically moored cylindrical buoy. IEEE J. Ocean. Eng. 2006, 31, 959–963. https://doi.org/10.1109/JOE.2006.880387
26. Yuan, N.; Xu, C.; Liu, Z. Experimental Study on the Spring-like Effect on the Hydrodynamic Performance of an Oscillating Water Column Wave Energy Converter. J. Mar. Sci. Eng. 2024, 12 (8), 1327. https://doi.org/10.3390/jmse12081327
27. Chen, S.G.; Chen, H.B.; Duan, Z.H.; et al. Progress in large-scale wave flume experimental research in China (2014–2024). Ocean Eng. 2025, 335, 121650. https://doi.org/10.1016/j.oceaneng.2025.121650
28. Stahlmann, A. Experimental and Numerical Modeling of Scour at Offshore Wind Turbines. Ph.D. Thesis, Franzius-Institute, Hannover, Germany, 2014.
29. Son, B.H.; Jeong, S.M.; Lee, C.Y. A hybrid CFD and potential flow motion analysis of spar buoys with damping-enhanced appendages. Water 2018, 10, 281. https://doi.org/10.3390/w1011281
30. Lindroth, S.; Leijon, M. Offshore wave power measurements—A review. Renew. Sustain. Energy Rev. 2011, 15, 4264-4276. https://doi.org/10.1016/j.rser.2011.07.070
31. Van Gent, M.R.A. The new delta flume for large-scale testing. In Proceedings of the 36th IAHR World Congress, The Hague, The Netherlands, 28 June-3 July 2015; pp. 1-4.
32. Pinguet, B.G.; Thiagarajan, K.; et al. Assessment of viscous damping of a solid heave disk for motion reduction of a floating circular cylinder. Appl. Ocean Res. 2024, 142, 103854. https://doi.org/10.1016/j.apor.2024.103854
33. Tao, L.; Molin, B.; Scolan, Y.M.; et al. Spacing effects on hydrodynamics of heave plates on offshore structures. J. Fluids Struct. 2007, 23, 1119–1136. https://doi.org/10.1016/j.jfluidstructs.2007.05.001
34. Faltinsen, Odd. Sea loads on ships and offshore structures. Vol. 1. Cambridge university press, 1993.
35. Chakrabarti, S.K. Handbook of Offshore Engineering; Elsevier: Oxford, UK, 2005.
36. Xue, C.; Guo, J.; Jiang, S.; Wang, Y.; Guo, Y.; Li, J. Performance Characteristics of Newly Developed Real-Time Wave Measurement Buoy Using the Variometric Approach. J. Mar. Sci. Eng. 2024, 12 (11), 2032. https://doi.org/10.3390/jmse12112032

 doi:10.20944/preprints202605.0930.v1

37. Kim, N.W.; Kim, Y.J.; Ha, Y.R. Experimental study of the free roll decay test for the evaluation of roll damping coefficients. J. Soc. Nav. Archit. Korea 2015, 52, 460–470. https://doi.org/10.3744/SNAK.2015.52.6.460
38. Bureau Veritas (BV). Rules for the Classification of Steel Ships; Bureau Veritas: Paris, France, 2011.
39. Cozijn, H.; Uittenbogaard, R.; Brake, E.T. Heave, roll and pitch damping of a deepwater CALM buoy with a skirt. In Proceedings of the 15th International Offshore and Polar Engineering Conference, Seoul, Korea, 19–24 June 2005; ISOPE: Cupertino, CA, USA, 2005; pp. 388–395.
40. Han, S.Y. Hydrodynamic Analysis and Numerical Modelling of Heave Plates for Offshore Structures. Ph.D. Thesis, Centrale Nantes, Nantes, France, 2025.
41. Chakrabarti, S.K. Empirical calculation of roll damping for ships and barges. Ocean Eng. 2001, 28, 915–932. https://doi.org/10.1016/S0029-8018(00)00036-6
42. Zou, S.; Abdelkhalik, O. A Numerical Simulation of a Variable-Shape Buoy Wave Energy Converter. J. Mar. Sci. Eng. 2021, 9 (6), 625. https://doi.org/10.3390/jmse9060625
43. Shi, Y.; Lin, J.; Zhuge, Z.; Zheng, R.; Zhang, J. Conceptual Design and Dynamic Analysis of a Wind–Wave Energy Converter with a Mass-Adjustable Buoy. J. Mar. Sci. Eng. 2024, 12 (8), 1460. https://doi.org/10.3390/jmse12081460
44. Yu, J.; Zhang, S.; Yang, W.; Xin, Y.; Gao, H. Design and Application of Buoy Single Point Mooring System with Electro-Optical-Mechanical (EOM) Cable. J. Mar. Sci. Eng. 2020, 8 (9), 672. https://doi.org/10.3390/jmse8090672